Dust Emissions on Mars From Phoenix Lidar Measurements in Relation to Local Meteorological Conditions

(article starts on next page)

Correspondence to:

M. Kahnert,
michael.kahnert@smhi.se

Dust Emissions on Mars From Phoenix Lidar Measurements in Relation to Local Meteorological Conditions

M. Kahnert[1,2] and **R. Ceolato[3]**

[1]Research Department, Swedish Meteorological and Hydrological Institute, Norrköping, Sweden, [2]Department of Space, Earth and Environment, Chalmers University of Technology, Gothenburg, Sweden, [3]ONERA, The French Aerospace Lab, Toulouse University, Toulouse, France

Abstract The diurnal cycle of dust aerosols on Mars is studied by analyzing lidar observations at the Phoenix landing site under cloud- and fog-free conditions and in the absence of elevated, long-range transported dust layers. There is a pronounced diurnal cycle in the dust-layer height with minimum heights of 4–6 km occurring between 11:00 and 17:00 local time. The ratio of the aerosol optical depth (AOD) within the lowermost 2 km to the total AOD reaches peak values at the same time. This can be explained by local dust emissions driven by the diurnal cycle of heating and cooling in the boundary layer. Analysis of wind and pressure measurements show that the gustiness of surface winds and the frequency of convective vortices undergo diurnal variations resembling those of AOD, indicating that these processes are the main drivers for local dust emissions.

Plain Language Summary Dust particles suspended in air are important for the radiative energy budget of Mars. By interacting with solar radiation, these aerosols impact the temperature, dynamics, and composition of the atmosphere, as well as the surface temperature of Mars. Dust aerosols are produced by wind-lifting processes ranging from small-scale eddies to planetary-scale dust storms, resulting in spatially and temporally varying concentrations. Here the focus is on the diurnal cycle of dust emissions as observed by the Phoenix lander. By jointly analyzing light-scattering observations by a lidar instrument and measurements of wind speed and air pressure, one can correlate the concentration of aerosols in air in proximity to the ground to meteorological processes. The results reveal distinct maxima in aerosol loads, the intensity of wind gusts, and the frequency of dust devils around local noon and early afternoon, and corresponding minima around midnight. This indicates that gustiness and dust devils, both fueled by solar heating during the day, are among the main causes for local dust emissions. During daytime the aerosols are concentrated at altitudes of 4–6 km. This can provide us with an indication for the degree of vertical mixing in the planetary boundary layer of Mars.

1. Introduction

Dust emissions on Mars are driven by processes ranging from local dust eddies to global dust storms. General circulation models account for lifting of dust by wind stress and by convective vortices (dust devils) (Kahre et al., 2006). The primary process in wind-stress generated dust is saltation, a predominantly horizontal flow of coarse particles in close proximity to the ground. These particles can, upon impact with the surface, transfer part of their momentum and kinetic energy to smaller particles, which can be kicked off the surface and remain airborne for extended periods of time (Kok et al., 2012). Saltation is initiated if the wind speed exceeds a threshold drag velocity known as the fluid threshold; it can be maintained if the wind speeds exceeds the so-called dynamic or impact threshold, which on Mars is an order of magnitude less than the fluid threshold (Kok, 2010a, 2010b). This hysteresis effect suggests that dust emission related to saltation can take place at wind speeds much lower than the fluid threshold if strong wind gusts assist in initiating the process (Kahre et al., 2006). Dust-devil lifting mainly depends on the vertical sensible heat flux, on the surface pressure, and the pressure at the top of the planetary boundary layer (PBL) (Kahre et al., 2006). Other mechanisms have been proposed to contribute to dust emissions, such as solid state greenhouse and photophoretic effects (Wurm et al., 2008) as well as forced convection within porous soils (de Beule et al., 2014).

Here, data from the Phoenix lander are analyzed with a focus on local dust emissions. Phoenix observations have previously been used to investigate clouds (Dickinson et al., 2010, 2011; J. A. Whiteway et al., 2009), dust aerosols (Daerden et al., 2015; Davy et al., 2009; Dickinson et al., 2011; Komguem et al., 2013), soil properties

(Shaw et al., 2009), turbulent heat fluxes (Davy et al., 2010), and dust devils (Ellehoj et al., 2010). The main novelty of the present study is that the diurnal cycle of local dust emissions as observed by the Phoenix lidar is analyzed in relation to the diurnal cycle of local meteorological conditions, particularly wind speed, gustiness, and the frequency of convective vortices. The analysis software and output data are made freely available (Kahnert & Ceolato, 2024).

2. Phoenix Data and Processing

Phoenix landed in Green Valley within the lowland region Vastita Borealis at 68.22°N, 125.75°W on 25 May 2008 (solar longitude $L_s = 77°$), 30 sols before summer solstice. Lidar observations are available until 24 October 2008 (148 sols after landing, solar longitude $L_s = 147°$).

The Phoenix lidar is a diode pumped, passively Q-switched Nd:YAG elastic backscatter lidar emitting 532 and 1,064 nm light into the zenith direction. The backscattered light was collected by a 10 cm telescope and detected as an analog signal by an avalanche photodiode (APD) at 1,064 nm, as well as by a photon multiplier tube at 532 nm as both an analog and a photon-counting signal. The analog signal was averaged, and the photon count accumulated over 2,048 pulses, resulting in a temporal resolution of 20.48 s. After averaging over height bins, the vertical resolution was 20 and 50 m for the analog and photon signals, respectively. Here, only data at 532 nm are analyzed, since the signal at 1,064 nm had a fairly low signal-to-noise ratio above 2 km altitude (Komguem et al., 2013). It was not possible to perform a relative calibration of the 532 and 1,064 nm channels, since the pulse energy at these two wavelengths depends on the instrument internal temperature, but the output energies of the laser pulses at the two wavelengths were not recorded with sufficient accuracy during the operation on Mars (Komguem et al., 2013). A more detailed description of the lidar instrument and calibration can be found in J. Whiteway et al. (2008).

The data processing routine largely follows the approach in Komguem et al. (2013), J. Whiteway et al. (2008).

1. Photon counting is used for detecting the weak signal at high altitudes. At low altitudes the analog signal is used, because the photon signal can be outside the detector's linear dynamic range. Thus the analog and photon signals need to be merged (with a smooth overlap region) around a critical altitude at which the nonlinearity becomes significant. We found that a smooth mearger can generally be obtained by considering the photon/analog ratio (normalized to unity at high altitudes) and its standard deviation σ_r, and by defining a nonlinearity threshold of $\max\{1.01, 1 + 3\sigma_r\}$. When exceeding this threshold, the photon signal is considered to be nonlinear.
2. The backscattered signal near the ground lies outside the telescope's field of view (FOV), followed by an altitude range of incomplete overlap between the returning laser pulse and the telescope FOV, while above that range the return signal lies fully within the FOV. The alignment of transmitter and receiver, hence the degree of incomplete overlap and its altitude range vary with temperature. A temperature-dependent correction has been applied to account for the incomplete capture of the return signal at low altitudes.
3. The data were averaged over time (up to a maximum of 1 hr).
4. The background signal was modeled by vertically averaging the photon counts at high altitudes (≥19 km), and the background was subtracted.
5. The observed lidar return signal is given by

$$S(z) = \frac{C}{z^2}\beta(z)\exp\left[-2\int_0^z \alpha(z')\,dz'\right],\tag{1}$$

where $\beta(z)$ and $\alpha(z)$ are the backscattering and extinction coefficients, respectively, at altitude z, and C is a calibration constant. The extinction coefficient was retrieved by the method of Fernald (1984) for a turbid atmosphere (Equation 10 in that paper), that is, scattering by aerosols dominates over scattering by air. The lidar equation was integrated from the top downwards with the constraint that the total aerosol optical depth (AOD) be equal to that observed by the Phoenix Surface Stereo Imager (SSI) (Lemmon et al., 2008). The SSI observations have been linearly interpolated in both time (based on 360 observations in total, typically 1–3 per sol), and in wavelength (between 451 and 671 nm) to match those of the Phoenix lidar.
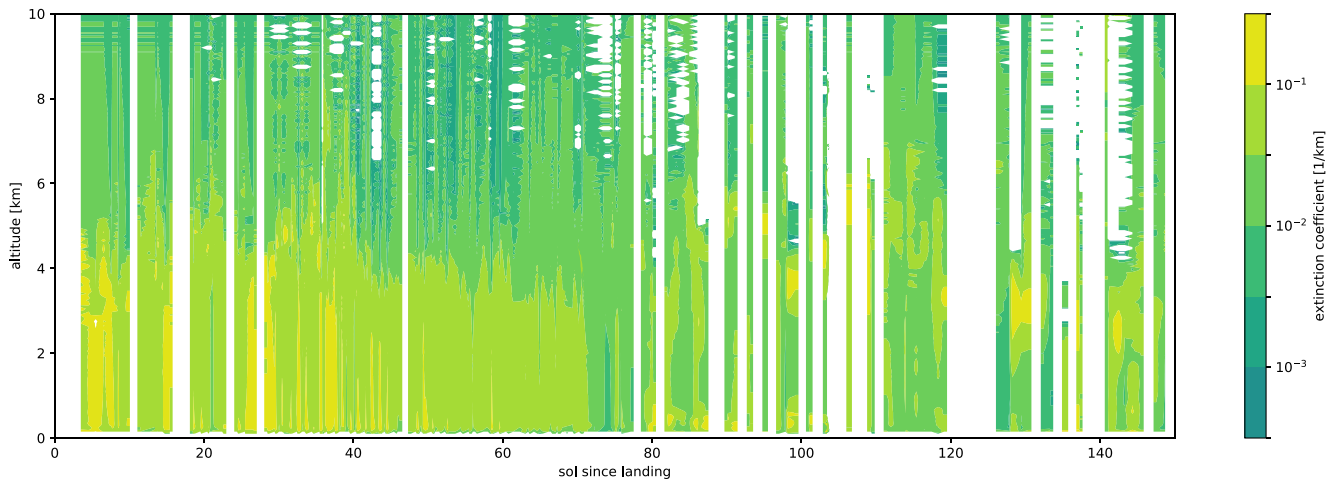
Figure 1. Time series of vertical profiles of the extinction coefficient.

6. During midday the background skylight often limited the detection of the backscattered laser light to low altitudes, typically $z \leq 7$ km, making it difficult to use the AOD measurement as a constraint in the extinction retrieval. This problem has been addressed by merging the low-altitude extinction profile with a high-altitudes background profile, either taken from the nearest nighttime observation, if available, or else taken to be an average over all nighttime profiles.

The Phoenix lander contained pressure, temperature, and wind instrumentation (Taylor et al., 2008). Here the wind and pressure measurements are analyzed. The horizontal wind speed u is a derived product from the telltale (TT) instrument (Holstein-Rathlou et al., 2010), which was mounted 1 m above the lander deck, hence 2 m above the surface. There are over 7,400 wind-speed data points available at irregular time intervals, usually clustered in time with an average rate of one observation every 2.3 ± 0.3 s. To investigate the diurnal cycle of gustiness, the wind-speed data are first divided into 12 two-hour time slots, that is, the slots comprise observation times at local midnight ± 1 hr, 2:00 a.m. ± 1 hr, etc. Within each subset, the data are further grouped into observations that are no more than 5 min apart. For each group that contains, at least, five observations $u(t)$, the maximum, mean, and standard deviation, $\max(u)$, $\bar{u}$, and $\sigma(u)$, are computed. Two dimensionless measures of gustiness are considered, namely, $\sigma(u)/\bar{u}$ and $|\max(u) - \bar{u}|/\bar{u}$. This approach gives the gustiness over a timescale of 5 min. To obtain the diurnal variation of the mean gustiness one computes $\langle \sigma(u)/\bar{u} \rangle$ and $\langle |\max(u) - \bar{u}|/\bar{u} \rangle$, where $\langle \cdots \rangle$ denotes the ensemble mean over each of the 2-hr time slots, and the ensemble comprises data from the entire 148-sol operation period.

The pressure sensor was near the lander deck (1 m above the ground) and had a temporal resolution of 2 s. Convective vortices passing the landing site can be detected by drops in surface pressure, as analyzed in detail in Ellehoj et al. (2010), who attributed convective vortices to pressure drops Δp with a magnitude of, at least, 0.3 Pa and a duration of 10–20 s. A stricter criterion with amplitudes >0.5 Pa had also been considered. Since the data of that study are not freely available, parts of the pressure-drop analysis are reproduced here. This reanalysis is based on Release 3 corrected pressure data of the Phoenix meteorological data product. The earlier Releases 1 and 2 contained incorrect values (Dickinson, 2008). An even more recent corrected data set by Kahanpää et al. (2020) only contains sample intervals of 512 s, which is too coarse for detecting convective vortices.

3. Results and Discussion

Figure 1 shows the retrieved extinction coefficient versus time and altitude. During the first half of the mission (sol ≤ 75) one typically sees a distinct dust layer extending to an altitude of 4–6 km, consistent with J. A. Whiteway et al. (2009); Komguem et al. (2013). A boundary-layer height extending up to 6 km is common on Mars (Petrosyan et al., 2011). Later in the summer (sol ≥ 80), there are numerous ice-cloud layers around 3–6 km and near-surface ice-fog. One reason is that the temperature started to decrease after sol 80 (Dickinson et al., 2011). Another reason is that clouds and fog were typically observed at night, and they dissipate in the morning (Dickinson et al., 2010). Before sol 75%, 66% of all measurements are daytime observations (between
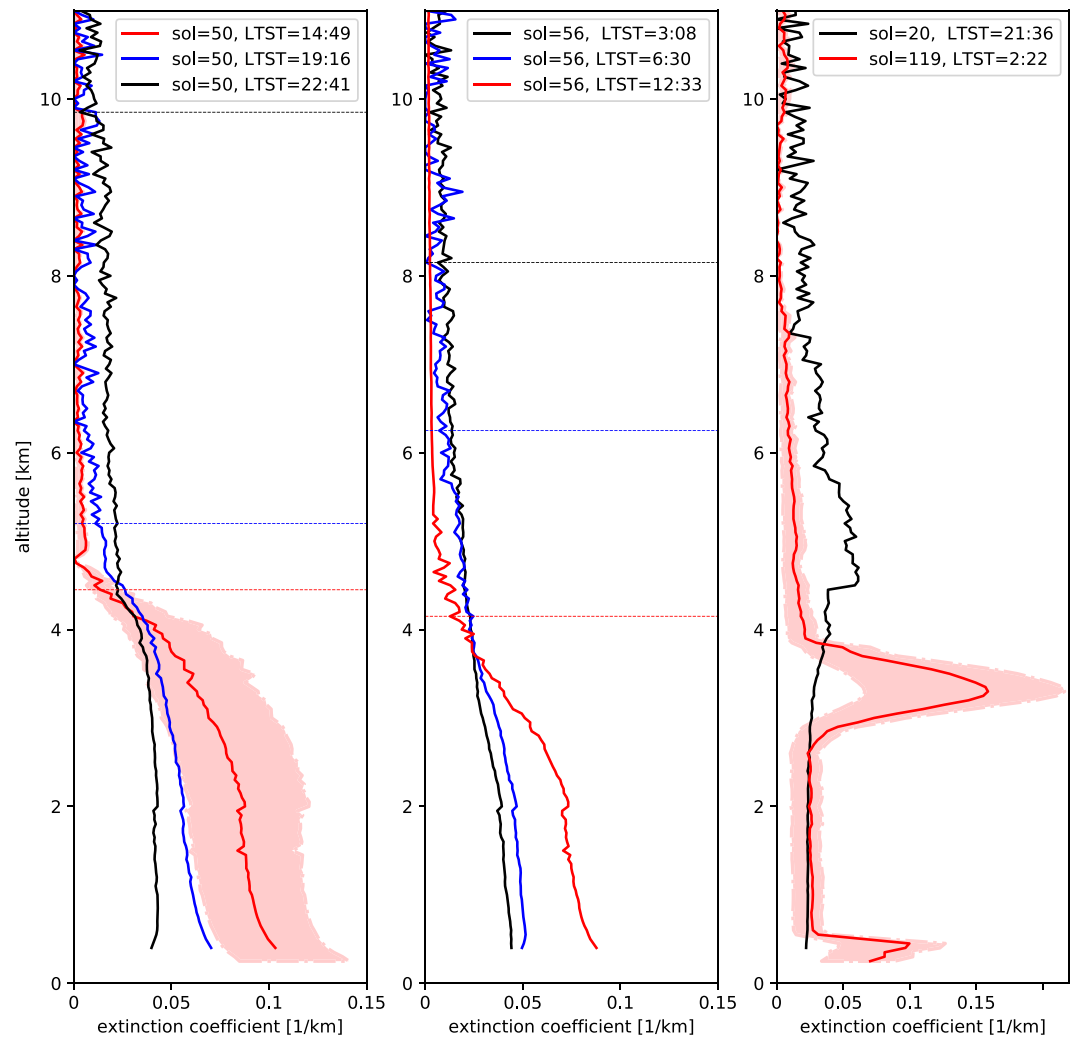
Figure 2. Vertical profiles of the extinction coefficient. Left: Cloud-free profiles observed on sol 50 at local true solar time (LTST) = 14:49 (red), 19:16 (blue), and 22:41 (black). Center: Cloud-free profiles on sol 56 at LTST = 3:08 (black), 6:30 (blue), and 12:33 (red). Right: Distinct cloud and fog layers on sol 119 at LTST = 02:22 (red), and an elevated dust layer at 5 km altitude on sol 20, LTST = 21:36 (black). Red shadings in the left and right panels show two examples of a retrieval-error analysis based on varying the column aerosol optical depth. Horizontal lines indicate dust-layer heights.

8:00 and 18:00 local true solar time (LTST)), while after sol 75%, 70% of all measurements are nighttime observations.

Figure 2 presents selected profiles of the extinction coefficient. The left and center panels illustrate a typical diurnal cycle of dust in the PBL. On sol 50 (left) during the day (red) there is a distinct dust layer extending up to 4–5 km, above which the extinction decreases sharply. During the evening (blue) and early night (black), this dust layer becomes less and less distinct. On sol 56 (center) late at night (black), the extinction coefficient is a smooth, decreasing function of altitude, while from the early morning (blue) until noon (red) it increases in the PBL.

The right panel in Figure 2 shows a typical example for a fog layer near the ground and a cloud layer between 3 and 4 km (red), and an elevated dust layer around 5 km (black). In Daerden et al. (2015) such elevated, long-range transported dust layers were investigated in detail. Measurements in which fog, clouds or elevated dust layers were present have been excluded in the analysis of the dust-layer height.

The sensitivity of the retrieved extinction coefficient to the AOD constraint has been tested by varying the AOD within a range $\pm\sigma$, where σ indicates the standard deviation of the AOD data record from the entire mission. The
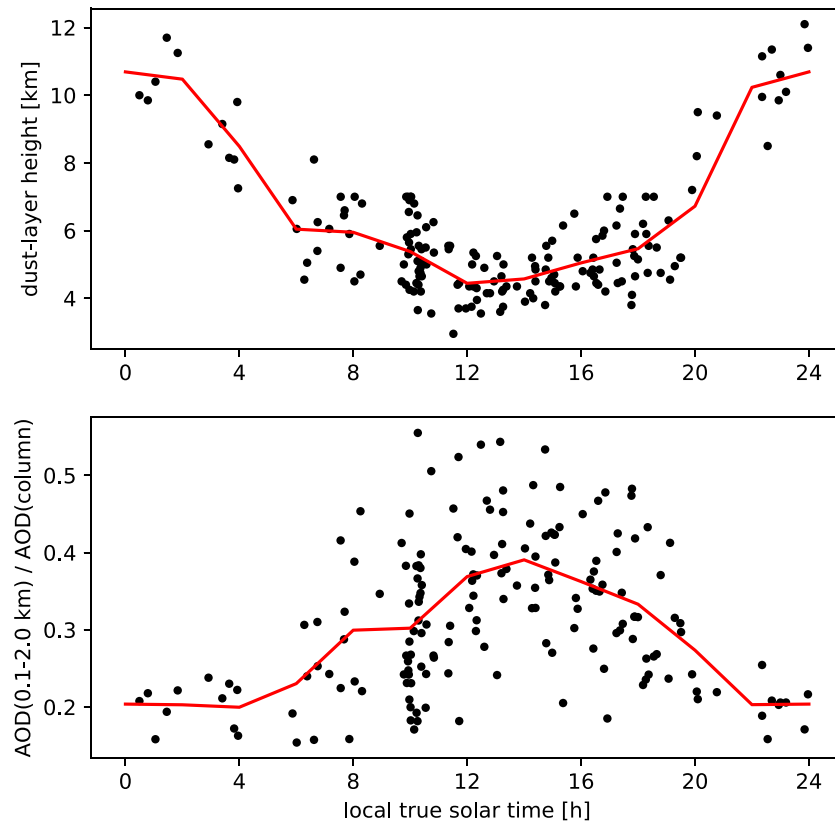
Figure 3. Diurnal variation of the dust-layer height (top), and optical depth at 532 nm between 0.1 and 2.0 km normalized by the total column aerosol optical depth (AOD) (bottom). The AOD between 0.1 and 2.0 km has been obtained from the lidar extinction, and the total AOD is based on Surface Stereo Imager observations. Symbols show data from all sols of the mission, red lines show 2-hr arithmetic mean values.

range of variation is shown for two cases in Figure 2 as a red shading. The retrieved extinction coefficient is quite sensitive to the AOD constraint, but the dust- and cloud-layer heights are highly robust.

The dust-layer height is quantified by defining $\alpha_{\max}^{\text{ground}}$ as the maximum extinction in the lowermost 1 km, and by defining the dust-layer height z_{dust} as that altitude at which the extinction has dropped below 15% of $\alpha_{\max}^{\text{ground}}$. For most daytime measurements, this is close to the altitude at which the extinction coefficient has just dropped to the background values in the free atmosphere. In the examples profiles in Figure 2 (left and center), z_{dust} is indicated by horizontal lines in the corresponding colors.

Figure 3 (top) shows the diurnal variation of z_{dust}. The symbols represent data from the entire 148-sol period that pass the selection criteria (no clouds, fog, or elevated dust). The red line shows arithmetic mean values for each 2-hr bin. Minimum values around 4–6 km are found between 11:00 and 17:00. During nighttime the vertical distribution of dust is more featureless, resulting in maximum layer heights up to 10–12 km between 22:00 and 2:00. This confirms that the diurnal variation of z_{dust}, which the examples in Figure 2 (left and center) suggested, is a phenomenon that can be found in the majority of lidar observations in the absence of clouds, fog, and elevated dust. The scattering of the data points about the mean is on the order of only ±1 km, indicating that these results are quite robust.

The retrieved extinction coefficient at 532 nm can be used to compute the AOD in the altitude range 0.1–2.0 km. To minimize the impact of possible long-term trends in AOD, we normalized this near-ground AOD by the total column AOD from the SSI instrument (interpolated in time and wavelength to match the lidar observations, as explained earlier). This displays a distinct diurnal variation (Figure 3, bottom).

Between 12:00 and 14:00 LTST, dust between 0.1 and 2.0 km contributes, on average, 40% to the total AOD, while around midnight this contribution drops to a minimum around 20%, most likely caused by dust deposition

and/or vertical mixing to higher altitudes. The daytime maximum suggests that there is an analogous peak in local dust emissions near the surface driven by a corresponding diurnal cycle in boundary-layer processes.

Lifting by near-surface wind stress is one important cause for injection of dust into the atmosphere (Kahre et al., 2006, 2017; Newman et al., 2002). If the drag velocity u_{drag} near the surface exceeds the fluid threshold u_{drag}^t, then a horizontal saltation flux is established. Very large particles are too heavy, while lifting of small particles is inhibited by cohesive forces binding the particles to the soil. The optimum particle size depends on the inter-particle cohesion I_p. A typical value on Mars (as well as on Earth) is $I_p = 6 \times 10^{-7}$ Nm$^{-1/2}$ (Newman et al., 2002). Inspection of, for example, Figure 1 in Newman et al. (2002) shows that for this value the minimum drag velocity is roughly $u_{drag}^t = 1.6$ m/s. Within the surface layer of the PBL, the wind at a height z can be modeled as (Garratt, 1992)

$$u(z) = \frac{u_{drag}}{k} \ln \frac{z}{z_0}, \qquad z \gg z_0, \tag{2}$$

where $k = 0.4$ is von Kármán's constant, and the surface-roughness scale z_0 is the height at which the wind velocity goes to zero. Assuming $z_0 = 0.01$ m (Newman et al., 2002) and $u_{drag}^t = 1.6$ m/s, this yields $u(z) = 21$ m/s at $z = 2$ m, where the TT instrument was mounted.

Figure 4 (top left) shows the lidar extinction coefficient at 150 m altitude versus TT wind speed for the whole 148-sol period (if the data pass the selection criteria). The TT measurements have been linearly interpolated in time to the instances of the lidar measurements. There is no clear trend of growing aerosol extinction with increasing wind speed, nor is there a diurnal trend in wind speed (top right). The TT wind velocities only vary within a narrow range between 2 and 7 m/s, which is well below the fluid threshold of 21 m/s.

Since the impact threshold can be 1 order of magnitude lower than the fluid threshold (Kahre et al., 2017; Kok, 2010a, 2010b), saltation can be initiated by strong wind gusts (Newman et al., 2002), and subsequently maintained by relatively low wind velocities. Figure 4 (center left) shows the diurnal cycle of the gustiness of the TT winds. The two measures of gustiness shown in the Figure were explained in Section 2. There is a pronounced gustiness maximum in the early afternoon, and a minimum at night. This mirrors the diurnal cycle of AOD, especially within the altitude range 0.1–2 km (Figure 3 bottom).

Figure 4 (center right, black line) shows the normalized frequency distribution, $f(u)$, of TT wind velocities, considering the entire TT data set (i.e., no time-interpolation to the instances of lidar measurements has been performed). $f(u)$ resembles a Weibull distribution (Seguro & Lambert, 2000)

$$f(u) = \frac{\kappa}{c}\left(\frac{u}{c}\right)^{\kappa-1} \exp\left[-\left(\frac{u}{c}\right)^{\kappa}\right], \tag{3}$$

where κ is a gustiness scale parameter (the lower κ, the higher the gustiness), and c is a velocity scale parameter. The red dashed line shows the best fit obtained with $\kappa = 2.6$ m/s and $c = 4.7$ m/s. Even the strongest wind gusts observed during the operation of Phoenix rarely exceeded 15 m/s.

This is confirmed in Figure 4 (bottom left), which shows the normalized frequency of wind gusts exceeding 10 m/s (black solid line) and 15 m/s (red dashed line). There is a diurnal cycle similar to that of the gustiness (center left), albeit confined to a narrower temporal range between 9:00 to 20:00 LTST. Wind gusts exceeding 10 m/s occur with a maximum frequency of 1%, while wind gusts stronger than 15 m/s are extremely rare. There was not a single occurrence of wind velocities exceeding the fluid threshold, 21 m/s, at 2 m above ground level. However, it was explained in Section 2 that the measurements and methodology used here for analyzing gustiness can only account for variations on a 5-min timescale.

For shorter timescales a higher gustiness is expected. For instance, the value of $\kappa = 2.6$ m/s obtained from the Weibull fit of the TT frequency distribution indicates a relatively low degree of gustiness. In Newman et al. (2002) it was proposed that κ in the range of 1–2 m/s (Lorenz et al., 1996) can be considered an upper limit for gustiness on minute timescales. Thus it is possible that strong gusts on shorter timescales could be responsible for initiating saltation, hence be a primary cause for the dust aerosols and its diurnal variation that are observed by the Phoenix lidar.
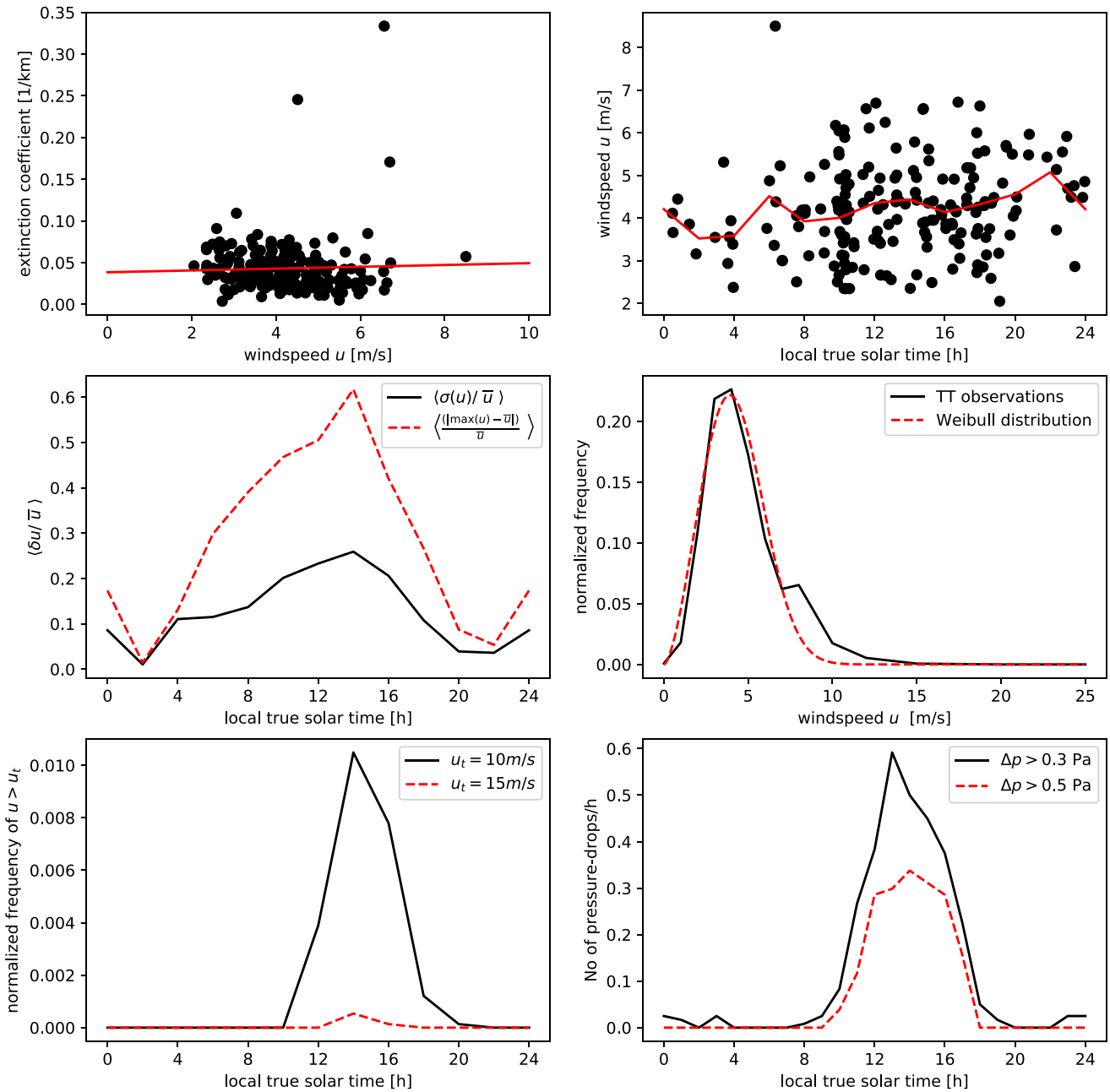
Figure 4. Top left: Extinction coefficient versus the telltale (TT) wind speed. The circles show the observations, the red line presents a linear fit to the data. Top right: diurnal variation of TT wind speed measurements (circles) and 2-hr arithmetic mean values (red line). Center left: diurnal variation of gustiness, as indicated in the legend. Center right: normalized frequency distribution of TT wind velocities (black solid line) and best-fit Weibull distribution (red dashed line). Bottom left: normalized frequency distribution of TT wind speeds exceeding a threshold u_t as indicated in the legend. Bottom right: Diurnal variation of the number of pressure drops per hour exceeding a prescribed threshold, as indicated in the legend.

Another important emission process is dust lifting by convective vortices (Kahre et al., 2006, 2017; Newman et al., 2002), which can be detected as pressure-drop events. Figure 4 (bottom right) shows the diurnal variation of the frequency of pressure-drop events at the Phoenix lander (averaged over the 148-sol period). Two pressure-drop thresholds have been considered, as explained in Section 2. The results are consistent with those in Elle-hoj et al. (2010). The diurnal cycle of convective vortices largely agrees with that of the near-surface AOD (Figure 3 bottom), although the latter is temporally broader.

4. Conclusions

Earlier landing missions, such as Curiosity (Vicente-Retortillo et al., 2018) or Perseverance (Smith et al., 2023), contained instrumentation for observations of the total atmospheric opacity. A diurnal variation of the total opacity has been observed (Smith et al., 2023) peaking around mid-sol, when also convective vortices peak (Newman et al., 2022). Unlike those previous missions, the Phoenix lidar provided a unique opportunity to observe the vertical distribution of dust, hence to make a distinction between local emissions and long-range transport. Here, vertical profiles of the extinction coefficient have been retrieved and analyzed for the 148-sol period of operation (from $L_s = 77°$ to $L_s = 147°$). Only data obtained in the absence of clouds, fogs, and elevated, long-range transported dust layers were considered, which made it possible to determine a dust-layer height z_{dust}. The main findings are:

1. z_{dust} undergoes a pronounced diurnal cycle, with minimum heights of 4–6 km during LTST between 11:00 and 17:00.
2. The relative contribution of the AOD in the lower part of the boundary layer (0.1–2.0 km, retrieved from the Phoenix lidar) to the total AOD (based on SSI observations) has a night-time minimum around 0.2 and a day-time maximum of 0.4 around noon.
3. The gustiness derived from the TT wind speed measurements as well as the frequency of pressure drop events display a diurnal variation that mirrors that of AOD(0.1–2.0 km)/AOD(column).

A plausible explanation is that local dust emissions are driven by saltation and/or convective vortices, which undergo diurnal variations driven by the diurnal cycle of heating and cooling. Saltation on Mars can be initiated by strong wind gusts on short time scales, yet it can be maintained by much calmer balanced winds (Kahre et al., 2017; Kok, 2010a, 2010b). This could explain the presence of near-surface dust and its daytime maximum even though the recorded wind speeds were below the fluid threshold.

GCM simulations that only account for wind-stress lifting fail to reproduce observed background dust during northern spring and summer (Basu et al., 2004; Newman et al., 2002). Convective vortices have been identified as an important emission process that contributes to background dust loading (Balme et al., 2003; Fisher et al., 2005). This process is accounted for in the NASA Ames Mars general circulation model (Kahre et al., 2006). Dust lifting by convective vortices is a local, small scale event, but it occurs ubiquitously over the entire planet (Kahre et al., 2017). The dust-devil activity at Phoenix, indicated by the frequency of pressure-drop events, displays a diurnal variation that approximately mirrors that of local dust emissions as reflected by the low-altitude AOD. In addition to a diurnal cycle, dust-devil emissions can also undergo an inter-annual variation (Vicente-Retortillo et al., 2018).

Data Availability Statement

The Python scripts (and their output data) for retrieving extinction coefficients, dust-layer heights, and dust-devil frequency have been published (Kahnert & Ceolato, 2024) under the Creative Commons Attribution 4.0 International license and can be downloaded at Zenodo, https://zenodo.org/records/10926997.

References

Balme, M. R., Whelley, P. L., & Greeley, R. (2003). Mars: Dust devil track survey in Argyre Planitia and Hellas basin. *Journal of Geophysical Research*, *108*(E8), 5086. https://doi.org/10.1029/2003je002096

Basu, S., Richardson, M. I., & Wilson, R. J. (2004). Simulation of the martian dust cycle with the GFDL Mars GCM. *Journal of Geophysical Research*, *109*(E11), E11006. https://doi.org/10.1029/2004je002243

Daerden, F., Whiteway, J. A., Neary, L., Komguem, L., Lemmon, M. T., Heavens, N. G., et al. (2015). A solar escalator on Mars: Self-lifting of dust layers by radiative heating. *Geophysical Research Letters*, *42*(18), 7319–7326. https://doi.org/10.1002/2015gl064892

Davy, R., Davis, J. A., Taylor, P. A., Lange, C. F., Weng, W., Whiteway, J., & Gunnlaugson, H. P. (2010). Initial analysis of air temperature and related data from the Phoenix MET station and their use in estimating turbulent heat fluxes. *Journal of Geophysical Research*, *115*(E3), E00E13. https://doi.org/10.1029/2009je003444

Davy, R., Taylor, P. A., Weng, W., & Li, P.-Y. (2009). A model of dust in the Martian lower atmosphere. *Journal of Geophysical Research*, *114*(D4), D04108. https://doi.org/10.1029/2008jd010481

de Beule, C., Wurm, G., Kelling, T., Küppler, M., Jankowski, T., & Teiser, J. (2014). The Martian soil as a planetary gas pump. *Nature Physics*, *10*(1), 17–20. https://doi.org/10.1038/nphys2821

Dickinson, C. (2008). Pds3 readme file. Retrieved from https://atmos.nmsu.edu/PDS/data/PDS4/PHX/met_bundle/document/pds3_readme.TXT

Dickinson, C., Komguem, L., Whiteway, J. A., Illnicki, M., Popovici, V., Junkermann, W., et al. (2011). Lidar atmospheric measurements on Mars and Earth. *Planetary and Space Science*, *59*(10), 942–951. https://doi.org/10.1016/j.pss.2010.03.004

Dickinson, C., Whiteway, J. A., Komguem, L., Moores, J. E., & Lemmon, M. T. (2010). Lidar measurements of clouds in the planetary boundary layer on Mars. *Geophysical Research Letters*, *37*(18), L18203. https://doi.org/10.1029/2010gl044317

Ellehoj, M. D., Gunnlaugsson, H. P., Taylor, P. A., Kahanpää, H., Bean, K. M., Cantor, B. A., et al. (2010). Convective vortices and dust devils at the Phoenix Mars mission landing site. *Journal of Geophysical Research*, *115*(E4), E00E16. https://doi.org/10.1029/2009je003413

Fernald, F. G. (1984). Analysis of atmospheric lidar observations: Some comments. *Applied Optics*, *23*(5), 652–653. https://doi.org/10.1364/ao.23.000652

Fisher, J. A., Richardson, M. I., Newman, C. E., Szwast, M. A., Graf, C., Basu, S., et al. (2005). A survey of Martian dust devil activity using Mars Global Surveyor Mars Orbiter Camera images. *Journal of Geophysical Research*, *110*(E3), E03004. https://doi.org/10.1029/2003je002165

Garratt, J. R. (1992). *The atmospheric boundary layer*. Cambridge University Press.

Holstein-Rathlou, C., Gunnlaugsson, H. P., Merrison, J. P., Bean, K. M., Cantor, B. A., Davis, J. A., et al. (2010). Winds at the Phoenix landing site. *Journal of Geophysical Research*, *115*(E5), E00E18. https://doi.org/10.1029/2009je003411

Kahanpää, H., Polkko, J., & Daly, M. (2020). The quality of the Mars Phoenix pressure data. *Planetary and Space Science*, *181*, 104818. https://doi.org/10.1016/j.pss.2019.104814

Kahnert, M., & Ceolato, R. (2024). Analysis program of Phoenix lidar and AOD data to retrieve the dust extinction coefficient; analysis of pressure-drop events [Dataset]. *Zenodo*. https://doi.org/10.5281/zenodo.10926997

Kahre, M. A., Murphy, J. R., & Haberle, R. M. (2006). Modeling the Martian dust cycle and surface dust reservoirs with the NASA Ames general circulation model. *Journal of Geophysical Research*, *111*(E6), E06008. https://doi.org/10.1029/2005je002588

Kahre, M. A., Murphy, J. R., Newman, C. E., Wilson, R. J., Cantor, B. A., Lemmon, M. T., & Wolff, M. J. (2017). The Mars dust cycle. In R. M. Haberle, R. T. Clancy, F. Forget, M. D. Smith, & R. W. Zurek (Eds.), *The atmosphere and Climate of Mars* (pp. 295–337). Cambridge University Press. https://doi.org/10.1017/9781139060172.010

Kok, J. F. (2010a). Difference in the wind speeds required for initiation versus continuation of sand transport on Mars: Implications for dunes and dust storms. *Physical Review Letters*, *104*(7), 074502. https://doi.org/10.1103/physrevlett.104.074502

Kok, J. F. (2010b). An improved parameterization of wind-blown sand flux on Mars that includes the effect of hysteresis. *Geophysical Research Letters*, *37*(12), L12202. https://doi.org/10.1029/2010gl043646

Kok, J. F., Parteli, E. J. R., Michaels, T. I., & Karam, D. B. (2012). The physics of wind-blown sand and dust. *Reports on Progress in Physics*, *75*(10), 106901. https://doi.org/10.1088/0034-4885/75/10/106901

Komguem, L., Dickinson, J. A. W. C., Daly, M., & Lemmon, M. T. (2013). Phoenix LIDAR measurements on Mars atmospheric dust. *Icarus*, *223*(2), 649–653. https://doi.org/10.1016/j.icarus.2013.01.020

Lemmon, M. T., Smith, P. H., Shinohara, C., Tanner, R., Woida, P., Shaw, A., et al. (2008). The Phoenix Surface Stereo Imager (SSI) investigation. In *39th annual lunar and planetary science conference* (p. 2156).

Lorenz, R. D., Lunine, J. I., Grier, J. A., & Fisher, M. A. (1996). Martian surface wind speeds described by the Weibull distribution. *Journal of Spacecraft and Rockets*, *33*(5), 754–756. https://doi.org/10.2514/3.26833

Newman, C. E., Hueso, R., Lemmon, M. T., Munguira, A., Vicente-Retortillo, Á., Apestigue, V., et al. (2022). The dynamic atmospheric and Aeolian environment of Jezero crater, Mars. *Science Advances*, *8*(21), eabn3783. https://doi.org/10.1126/sciadv.abn3783

Newman, C. E., Lewis, S. R., Read, P. L., & Forget, F. (2002). Modeling the Martian dust cycle 1. Representations of dust transport processes. *Journal of Geophysical Research*, *107*(E12), 5123. https://doi.org/10.1029/2002je001910

Petrosyan, A., Galperin, B., Larsen, S. E., Lewis, S. R., Määtänen, A., Read, P. L., et al. (2011). The Martian atmospheric boundary layer. *Reviews of Geophysics*, *49*(3), RG3005. https://doi.org/10.1029/2010rg000351

Seguro, J. V., & Lambert, T. W. (2000). Modern estimation of the parameters of the Weibull wind speed distribution for wind energy analysis. *Journal of Wind Engineering and Industrial Aerodynamics*, *85*(1), 75–84. https://doi.org/10.1016/s0167-6105(99)00122-1

Shaw, A., Arvidson, R. E., Bonitz, R., Carsten, J., Keller, H. U., Lemmon, M. T., et al. (2009). Phoenix soil physical properties investigation. *Journal of Geophysical Research*, *114*(E1), E00E05. https://doi.org/10.1029/2009je003455

Smith, M. D., Martínez, G. M., Sebastián, E., Lemmon, M. T., Wolff, M. J., Apéstigue, V., et al. (2023). Diurnal and seasonal variations of aerosol optical depth observed by MEDA/TIRS at Jezero crater, Mars. *Journal of Geophysical Research: Planets*, *128*(1), e2022JE007560. https://doi.org/10.1029/2022je007560

Taylor, P. A., Catling, D. C., Daly, M., Dickinson, C. S., Gunnlaugsson, H. P., Harri, A.-M., & Lange, C. F. (2008). Temperature, pressure, and wind instrumentation in the Phoenix meteorological package. *Journal of Geophysical Research*, *113*(E3), E00A10. https://doi.org/10.1029/2007je003015

Vicente-Retortillo, Á., Martínez, G. M., Renno, N., Newman, C. E., Ordonez-Etxeberria, I., Lemmon, M. T., et al. (2018). Seasonal deposition and lifting of dust on Mars as observed by the Curiosity Rover. *Scientific Reports*, *8*(1), 17576. https://doi.org/10.1038/s41598-018-35946-8

Whiteway, J., Daly, M., Carswell, A., Duck, T., Dickinson, C., Komguem, L., & Cook, C. (2008). Lidar on the Phoenix mission to Mars. *Journal of Geophysical Research*, *113*(E3), E00A08. https://doi.org/10.1029/2007je003002

Whiteway, J. A., Komguem, L., Dickinson, C., Cook, C., Illnick, M., Seabrook, J., et al. (2009). Mars water-ice clouds and precipitation. *Science*, *325*(5936), 68–70. https://doi.org/10.1126/science.1172344

Wurm, G., Teiser, J., & Reiss, D. (2008). Greenhouse and thermophoretic effects in dust layers: The missing link for lifting of dust on Mars. *Geophysical Research Letters*, *35*(10), L10201. https://doi.org/10.1029/2008gl033799